

Article

# Using Geomatic Techniques to Estimate Volume–Area Relationships of Watering Ponds

Ubaldo Marín-Comitre <sup>\*</sup>, Álvaro Gómez-Gutiérrez <sup>id</sup>, Francisco Lavado-Contador <sup>id</sup>,  
Manuel Sánchez-Fernández <sup>id</sup> and Alberto Alfonso-Torreño <sup>id</sup>

Institute for Sustainable Land Development (INTERRA), University of Extremadura, 10071 Cáceres, Spain; alvgo@unex.es (Á.G.-G.); frlavado@unex.es (F.L.-C.); msf@unex.es (M.S.-F.); albertoalfonso@unex.es (A.A.-T.)

\* Correspondence: umarin@unex.es

**Abstract:** Watering ponds represent an important part of the hydrological resources in some water-limited environments. Knowledge about their storage capacity and geometrical characteristics is crucial for a better understanding and management of water resources in the context of climate change. In this study, the suitability of different geomatic approaches to model watering pond geometry and estimate pond-specific and generalized volume–area–height (V–A–h) relationships was tested. Terrestrial structure-from-motion and multi-view-stereo photogrammetry (SfM-MVS), terrestrial laser scanner (TLS), laser-imaging detection and ranging (LIDAR), and aerial SfM-MVS were tested for the emerged terrain, while the global navigation satellite system (GNSS) was used to survey the submerged terrain and to test the resulting digital elevation models (DEMs). The combined use of terrestrial SfM-MVS and GNSS produced accurate DEMs of the ponds that resulted in an average error of 1.19% in the maximum volume estimation, comparable to that obtained by the TLS+GNSS approach (3.27%). From these DEMs, power and quadratic functions were used to express pond-specific and generalized V–A–h relationships and checked for accuracy. The results revealed that quadratic functions fit the data particularly well ( $R^2 \geq 0.995$  and  $NRMSE < 2.25\%$ ) and can therefore be reliably used as simple geometric models of watering ponds in hydrological simulation studies. Finally, a generalized V–A power relationship was obtained. This relationship may be a valuable tool to estimate the storage capacity of other watering ponds in comparable areas in a context of data scarcity.

**Keywords:** livestock watering pond; volume–area relationship; structure-from-motion photogrammetry (SfM); LIDAR; terrestrial laser scanner (TLS); global navigation satellite system (GNSS)



**Citation:** Marín-Comitre, U.; Gómez-Gutiérrez, Á.; Lavado-Contador, F.; Sánchez-Fernández, M.; Alfonso-Torreño, A. Using Geomatic Techniques to Estimate Volume–Area Relationships of Watering Ponds. *ISPRS Int. J. Geo-Inf.* **2021**, *10*, 502. <https://doi.org/10.3390/ijgi10080502>

Academic Editor: Wolfgang Kainz

Received: 10 June 2021

Accepted: 23 July 2021

Published: 26 July 2021

**Publisher's Note:** MDPI stays neutral with regard to jurisdictional claims in published maps and institutional affiliations.



**Copyright:** © 2021 by the authors. Licensee MDPI, Basel, Switzerland. This article is an open access article distributed under the terms and conditions of the Creative Commons Attribution (CC BY) license (<https://creativecommons.org/licenses/by/4.0/>).

## 1. Introduction

Watering ponds are the main source of drinking water for livestock in the rangelands of the southwestern (SW) Iberian Peninsula [1]. Most of these ponds consist of small earth dams that collect surface runoff from ephemeral streams, with pond sizes rarely exceeding 1 ha [2,3]. Understanding the hydrological functioning of this type of infrastructure is crucial for efficient water management in extensive livestock farms, especially in semi-arid areas, where water resources are often scarce.

Simulation of water-level fluctuation through water-balance models is a frequently used approach to analyze the hydrological dynamics of small water bodies [4]. In these models, the temporal variation of both the stored volume (V) and the flooded area (A) in the water body are often required inputs. However, due to the difficulty of directly monitoring V and A, these are usually calculated from the height of water surface above the pond bottom (h), using predetermined V–h and A–h relationships [5]. It is usual to define these relationships using simple geometric models. The most frequent models use power or quadratic functions to express the V–h and A–h relationships, which has been successfully tested in simulation studies of reservoirs [6], wetlands [7,8], and lakes [9].

V–A relationships (usually defined by power functions) also can be used to model the morphometry of individual water bodies in hydrological simulation studies [10–13]. In fact, this is the method implemented in the widely used SWAT model [14] to morphologically define reservoir-type elements.

V–A–h relationships can be developed for a particular pond if a detailed bathymetry is available [4]. The most common methods traditionally used to survey the bathymetry of small water bodies include total station, the global navigation satellite system (GNSS), and meter stick [15]. However, the use of these methods may be too costly, labor intensive, and time consuming, especially when a large number of water bodies have to be surveyed.

Laser-based survey techniques evolved quickly in the last decades, and they have been widely used to provide topographic data for hydrological applications [16]. At this point, we may differentiate between aerial and terrestrial systems, known as laser-imaging detection and ranging (LIDAR) and terrestrial laser scanner (TLS), respectively. There are freely available national LIDAR datasets (e.g., the National Geographic Information Center in Spain [17]), but their use to produce reliable V–A–h relationships that can be used in hydrological studies is limited [8,18]. Terrestrial systems (fixed or mobile) may capture terrain characteristics with higher resolution and accuracy than aerial sensors [16,19], but the cost and operation of these instruments are important limiting factors [15,19,20].

On the other hand, the characteristics of livestock watering ponds in the SW Iberian Peninsula (size, water depth, and turbidity) make unsuitable the use of technologies commonly used to survey submerged areas, such as bathymetric green airborne LIDAR [21], bathymetric sonar on manned boat [22], or through-water TLS [23]. Nonetheless, the rapid development in recent years of low-cost mobile platforms such as unmanned aerial vehicles (UAVs) and unmanned surface vehicles (USVs), with increasing use in surveying applications, is making it possible to solve many of the drawbacks associated with traditional surveying techniques in the presence of shallow and turbid waters. For example, a small unmanned vessel can be equipped with a bathymetric sonar to survey the submerged terrain [24], while the emerged areas can be surveyed using UAV photogrammetry [25–29].

Low-cost and efficient methodological alternatives based on satellite data have been proposed by several authors to estimate V–A–h relationships for lakes or reservoirs [30–32]. These methods use simultaneous measurements of the flooded area and the water level, the latter being determined in situ [12,33,34] or by means of satellite altimetry [35–37]. However, although remote-sensing techniques have proved useful for detecting and mapping small ponds [38], these approaches do not provide sufficient accuracy for topo-bathymetric applications in water bodies with a surface area <1 ha [39–41].

Some recent developments in 3D photo-reconstruction techniques, such as the concurrent use of structure-from-motion (SfM; [42]) and multi-view-stereo (MVS; [43]), have contributed to the rapid and cheap production of high-resolution point clouds with similar accuracy to that provided by TLS and conventional photogrammetry [44–47]. Livestock watering ponds in the SW Iberian Peninsula seem to be suitable for SfM-MVS techniques, as they commonly lack vegetation, and the survey may be carried out at the end of the summer, when they are shallow or completely dry. Additionally, these ponds are usually very small, facilitating the acquisition of images from the ground. Examples in the literature on the use of SfM-MVS techniques to model the geometry of water bodies and estimate the V–A–h relationships are scarce. To our knowledge, the only example is that of Langhammer et al. [18], who applied SfM-MVS to images acquired using a UAV platform to estimate the V–h and A–h relationships for an abandoned montane reservoir. Hence, the suitability of terrestrial SfM-MVS photogrammetry to model water-pond terrain has not been tested yet.

The existence of water in the ponds, sometimes throughout the year, makes it difficult to acquire complete and accurate terrain models, requiring combined approaches for the exposed and submerged terrain [48]. In the wider context of hydrology and fluvial geomorphology, examples of the use of a single technique to register exposed and submerged terrain are scarce and have shown significant limitations [49].

Small water bodies like livestock watering ponds are not usually regarded as part of the hydrological system by water agencies, but the accumulation of large numbers of these water bodies can impact the hydrology, and can be the cause of water conflicts because they take water from the available stream flow [50,51]. Therefore, information about the storage capacity of these water bodies is essential for decision-making processes regarding planning and management of water resources. In this regard, regional V–A relationships are often used to estimate and monitor the volume of water stored in non-surveyed water bodies based on data of flooded areas, which can be obtained from databases [52], topographic maps [53], high-resolution aerial photographs [54], satellite imagery [50], or LIDAR datasets [55].

For any of the above applications, a frequent approach in studies at the basin or regional scale is to fit a common geometric model from the known bathymetry of a set of reference water bodies and apply the function thus obtained to the rest of the water bodies in a given region, assuming that the model parameters remain approximately constant if the geomorphological context is uniform [10–13,50,52,55–60].

On the above considerations, the objectives of this paper are:

1. To apply and compare different geomatic approaches and techniques to model the topography of small watering ponds (terrestrial or close-range SfM-MVS, aerial SfM-MVS, GNSS, LIDAR, and TLS). Specifically, the suitability of terrestrial SfM-MVS photogrammetry was tested, as it could be a low-cost, high-accuracy alternative to laser technologies or more time-consuming GNSS surveys. Tips on the use of this approach are also provided;
2. To assess the overall suitability of power and quadratic functions to describe watering-pond geometry by means of pond-specific V–A–h relationships. These relationships could be a valuable tool to be used as a geometric model of watering ponds in hydrological simulation studies;
3. To obtain a generalized V–A relationship from the surveys carried out at eight small watering ponds that may be used to estimate the storage capacity of other watering ponds in similar rangeland areas.

The paper has been organized in five sections. The first section presents the motivation and objectives of the study. In Section 2, the methodology is presented, including a description of the study area, the field surveys, and the methods used to derive the V–A–h relationships of the ponds. In Section 3, the results of the geomatic measurements are presented, as well as the resulting V–A–h relationships. Finally, Sections 4 and 5 include the discussion of the results and the main conclusions, respectively.

## 2. Materials and Methods

### 2.1. Study Area

For this work, two privately owned farms (Parapuños and La Brava) and a communal farm (Dehesa Boyal Monroy) located in the SW Iberian Peninsula were selected as study areas (Figure 1). They are representative of the *dehesa* land-use system, an agro-silvo-pastoral system characterized by the presence of open wooded pasturelands of evergreen oaks (*Quercus ilex* subsp. *ballota* and *Q. suber*). These rangelands dominate the landscape of SW Iberia (Figure 1a) and are considered of high natural value in Europe, due to the wide range of ecosystem services they provide [61].

The study farms share the dominant geomorphological characteristics of the rangelands in the SW Iberian Peninsula: the landscape is characterized by gently undulating erosion surfaces, incised by small channels with ephemeral flow, giving rise to increasing slope gradients as approaching the main rivers; with slates and greywackes being the predominant bedrocks. The soils are generally shallow, prevailing Cambisols and Leptosols [62]. The climate is Mediterranean, with a humid season from October to May and a pronounced dry and hot season (June–September), particularly in July and August. Rainfall shows a high temporal variability, both annually and inter-annually [63]. Livestock rearing is the main land use in the study farms.

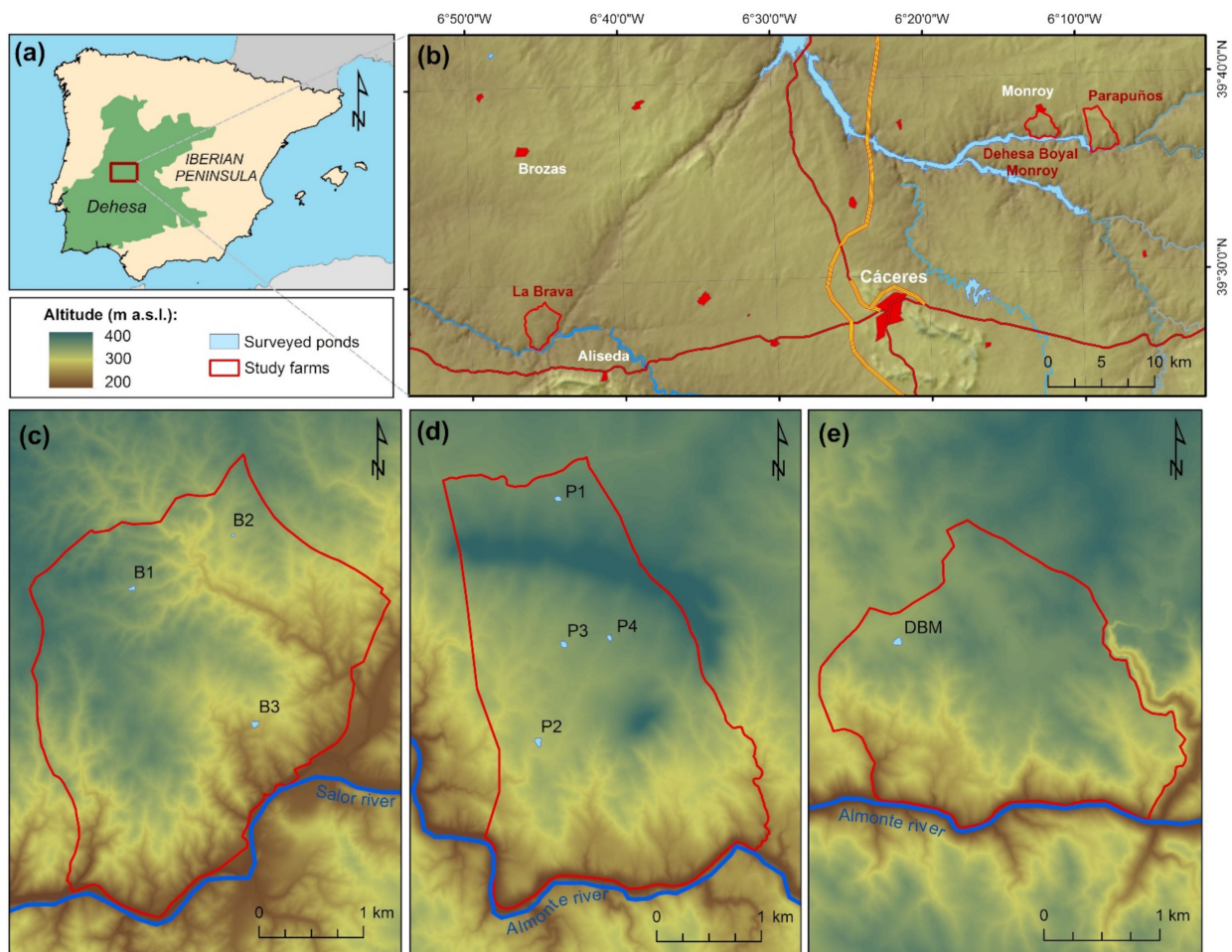


**Figure 1.** (a) Area where dehesas are widespread in the Iberian Peninsula (based on [64]); (b) location of the study farms, and location of the surveyed ponds in the La Brava (c), Parapuños (d), and Dehesa Boyal Monroy (e) farms.

## 2.2. Surveying Watering-Pond Geometry

Throughout the study farms, several ponds were selected in which the water depth was low enough to allow point collection by wading: P1, P2, P3, and P4 at Parapuños farm; B1, B2, and B3 at La Brava farm; and DBM at Dehesa Boyal Monroy farm (Figure 1c–e).

Several geomatic techniques were applied and combined to model the geometry of the selected watering ponds (Table 1). As stated before, watering ponds present areas that usually remain submerged even at the end of the hydrological year, requiring the support of GNSS or any other technique to survey the inundated areas. In most cases, the submerged areas show an almost flat and horizontal surface that would be easily modeled by surveying a few points. Specifically, terrestrial or close-range SfM-MVS photogrammetry (supported on GNSS for the submerged terrain) was used for ponds B1 and B2; LIDAR and GNSS data were used for ponds P1, P2, P3, and B3; and aerial SfM-MVS photogrammetry (supported on GNSS for the submerged areas) was used for pond DBM. Finally, pond P4 was surveyed by combining TLS and GNSS for the exposed and submerged terrain, respectively. These techniques were used to survey the topography and produce a DEM of each watering pond. Then, the DEMs were tested using independent check control points (CCPs) previously surveyed with a GNSS RTK device. Well-known and state-of-the-art error metrics were calculated comparing the CCPs and the DEMs: the root mean square error (RMSE), the mean error (ME), and the standard deviation of error (STDE).

**Table 1.** Surveying approach for the emerged and submerged terrain of the watering ponds. SfM-MVS: structure-from-motion and multi-view-stereo photogrammetry; GNSS: global navigation satellite system; LIDAR: laser-imaging detection and ranging; TLS: terrestrial laser scanner.

Name	Farm	Emerged Terrain	Submerged Terrain
B1	La Brava	Close-range SfM-MVS	GNSS
B2	La Brava	Close-range SfM-MVS	GNSS
B3	La Brava	LIDAR	GNSS
P1	Parapuños	LIDAR	GNSS
P2	Parapuños	LIDAR	GNSS
P3	Parapuños	LIDAR	GNSS
P4	Parapuños	TLS	GNSS
DBM	Dehesa Boyal Monroy	Aerial SfM-MVS	GNSS

Field surveys of ponds B1 and B2 were carried out in late summer 2019, when the ponds were at their lowest water level (just a few centimeters; Figure 2a). At this time, a GNSS antenna tied to a survey rod could be used to survey the topography of the submerged surface (Figure 2). Two Emlid Reach RS antennas were operated as base and rover, respectively. The fixed base station registered coordinates from satellites and sent corrections through a long-range (LoRa) link to the rover antenna, which performed in real-time kinematic (RTK) and fixed-solution status modes. Twenty artificially marked additional points (Figure 2b) were recorded in the emerged area, also by using the rover GNSS in the RTK mode. These points performed later as ground control points (GCPs, which were used to scale and georeference the model and refine camera calibration parameters,  $n = 15$ ) and CCPs (i.e., check control points; these points were not used in the composition of the model, but rather to check the geometrical accuracy of the 3D model,  $n = 5$ ) for the SfM-MVS processing.



**Figure 2.** (a) GNSS data acquisition in the submerged area of pond P1, and (b) marks of two CCPs at the bank and the bottom of pond B1.

In order to survey the emerged surface in detail, photographs were acquired around the pond with a Canon 550D digital single-lens reflex camera (DSLR), drawing a convergent image network geometry (Figure 3). The Canon sensor had  $5184 \times 3456$  pixels, and the focal length was fixed to 35 mm. The Pix4Dmapper pro software (v. 4.5.6) was used for the photogrammetric processing with parameters and specifications shown in Table 2. The GCPs were marked after the initial alignment, then the model was reoptimized to support the refinement of camera parameters. At this point, the layer of water was masked from the point cloud. The resulting point cloud for the emerged terrain (Figure 4a–d) was merged

with the GNSS data acquired over the submerged surface, and the resulting point cloud was used to produce a DEM of each pond. This task was carried out with the CloudCompare software package and the rasterize tool. This tool allows an estimation of the Z-value for a pixel (i.e., a XY location) that contains several Z-values (which is typical in high-density regions of a point cloud) and, at the same time, allows the interpolation of values in low point-density regions. A pixel size of 0.2 m was defined for the resulting DEMs.

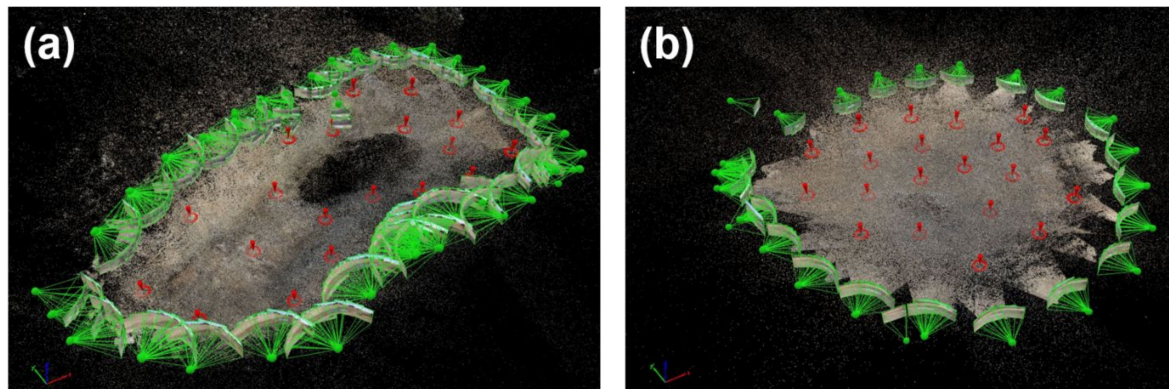


**Figure 3.** Convergent image network geometry (every camera pose is shown in green), sparse point cloud, and GCPs (in red) for (a) pond B1 and (b) pond B2.

**Table 2.** Pix4Dmapper Pro parameters used for the photo-reconstruction of watering ponds.

Workflow Stage	Parameter	Value
		Terrestrial (B1, B2)/Aerial
Initial processing	Image scale	Complete
	Image scale	1 (original size)
Dense point cloud	Point density	High (slow)
	Minimum number of matches	3

Watering ponds P1, P2, P3, and B3 were surveyed using the GNSS in RTK mode for the submerged surface, while the emerged topography was obtained from the LIDAR dataset provided by the Spanish National Geographic Information Centre [17] (e.g., Figure 5). This dataset shows a point density of  $0.5 \text{ pts}\cdot\text{m}^{-2}$  and was acquired using a Leica ALS50 sensor. Both point datasets were merged together and then the topographic surface was modelled using the interpolation algorithm *topo to raster* [65] within the ArcGIS software (10.5), producing a DEM for each pond with a pixel size of 0.5 m (Figure 4b). Additionally, five points were recorded with the GNSS RTK system and performed as CCPs in order to evaluate the accuracy of the resulting DEMs (i.e., these points were not used in the production of the DEM). This quantification includes the error of the instrument techniques (i.e., LIDAR and GNSS) and the interpolation technique (i.e., the *topo to raster* algorithm).

Watering pond DBM was surveyed using a fixed-wing UAV (Ebee classic by Sensefly) with a Sony WX220 sensor on board (18 Mpx) in early summer. At this time, a water layer of a couple of decimeters covered the bottom of the pond. The topography of DBM was obtained using a dataset previously acquired by Alfonso-Torreño et al. [66] for the exposed terrain and, again, the submerged terrain was surveyed by means of the GNSS RTK system. A total of 84 points were collected by means of the GNSS, from which 79 were used in combination with the point cloud derived from SfM-MVS to generate a DEM, with the remaining 5 points employed as CCPs. A pixel size of 0.2 m was selected for the resulting DEM.

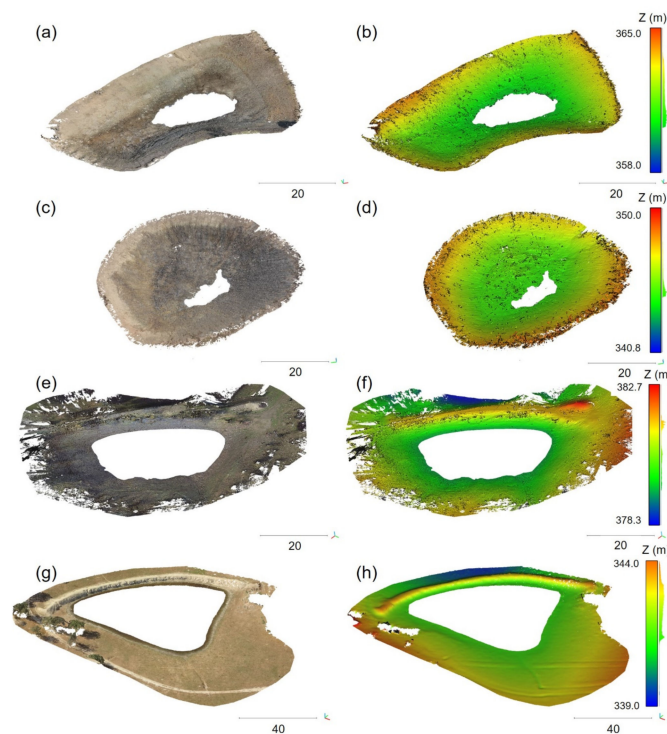


**Figure 4.** Point clouds showing the RGB values and elevation for B1 (a,b), B2 (c,d), P4 (e,f), and DBM (g,h). Note that B1 and B2 were surveyed using terrestrial SfM-MVS photogrammetry, P4 was surveyed by means of TLS, and DBM was surveyed using aerial SfM-MVS photogrammetry. Scale bars = 20 m for (a–f) and 40 m for (g,h).

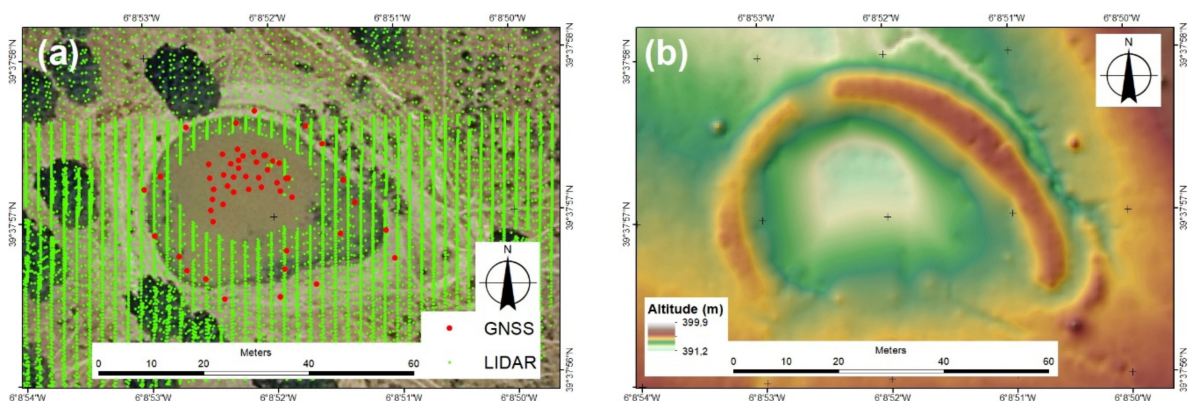


**Figure 5.** (a) Datasets used to model the topography of pond P1 and (b) resulting DEM for pond P1.

Finally, watering pond P4 was surveyed combining a TLS (Faro Focus 3D X330) and the GNSS in RTK mode for the emerged and submerged areas, respectively. A total of 15 stations were registered together using a set of artificial spheres (diameter of 14.5 cm). In order to georeference the TLS data, 8 artificial points were marked and surveyed with the GNSS. Finally, 706 points were surveyed in the submerged area by means of the GNSS. Ten additional locations were surveyed in the study area to be used as CCPs to evaluate the quality of the resulting DEM. This DEM was produced by merging together the TLS cloud and the GNSS data, using the rasterize tool within CloudCompare software and defining an output pixel size of 0.2 m.

Maximum uncertainties in the estimation of the water-storage capacity of the ponds were calculated from the maximum area of each pond and the vertical error estimated for each approach, using the following equation:

$$V_E = RMSE_z \cdot A_{max}, \quad (1)$$

where  $V_E$  is the error associated to the estimation of the water storage capacity of a pond,  $RMSE_z$  is the root mean square error of the Z coordinate calculated for the method used to model the topography, and  $A_{max}$  is the maximum area of the pond. Specifically, the  $RMSE_z$  was calculated using the CCPs surveyed by the GNSS RTK system, while  $A_{max}$  was estimated using the DEM and the altitude of the spillway (overflow channel).

### 2.3. Obtaining Volume–Area–Height Relationships

For each of the study ponds, V and A values were calculated at intervals of 10 cm in height (over the entire depth range) from the DEM of each pond using the geoprocessing tools of the ArcGIS v10.5 (ESRI) software. In each case, the values of V and A calculated at the maximum water height (i.e., at the elevation of the pond spillway) were assigned the maximum volume ( $V_{max}$ ) and the maximum surface area ( $A_{max}$ ) of the pond, respectively. Then, Microsoft Excel software was used to derive pond-specific V–h, A–h and V–A relationships by fitting (by least squares) power and quadratic functions of the forms:

$$y = \alpha x^\beta, \quad (2)$$

$$y = ax^2 + bx + c, \quad (3)$$

with  $\alpha$ ,  $\beta$ ,  $a$ ,  $b$ , and  $c$  being the adjustment parameters. The goodness of fit of the resulting relationships was determined with the coefficient of determination ( $R^2$ ) and the normalized root mean square error (NRMSE). The latter was calculated for volume (NRMSE<sub>V</sub>) or area (NRMSE<sub>A</sub>) as follows:

$$NRMSE_V = \frac{100}{V_{max}} \sqrt{\frac{1}{k} \sum_{i=1}^k (V_{DEM} - V_F)_i^2}, \quad (4)$$

$$NRMSE_A = \frac{100}{A_{max}} \sqrt{\frac{1}{k} \sum_{i=1}^k (A_{DEM} - A_F)_i^2}, \quad (5)$$

where  $i$  is the index number for the pond water level,  $k$  is the total number of pond water levels,  $V_{DEM}$  is the pond volume derived from the DEM at water level  $i$ ,  $V_F$  is the pond volume derived from the fitted function (either the power or the quadratic) at water level  $i$ ,  $A_{DEM}$  is the pond area derived from the DEM at water level  $i$ , and  $A_F$  is the pond area derived from the fitted function at water level  $i$ .

In order to obtain generalized V–h, A–h, and V–A relationships that may be used at the regional scale, the values of V, A, and h (obtained every 10 cm depth) from all study ponds were represented together and fitted equally by means of power and quadratic functions.

Finally, a generalized V–A relationship was also derived by fitting a power function to the  $V_{max}$  and  $A_{max}$  values of the study ponds, to test whether sufficiently reliable  $V_{max}$  values could be obtained based solely on the  $A_{max}$  values of the study ponds.

## 3. Results

### 3.1. Suitability of Terrestrial and Aerial SfM-MVS Photogrammetry to Model the Topography of Small Watering Ponds

The point clouds produced for the emerged parts of ponds B1 and B2 showed huge amounts of points and resulted in point densities of 19,143 and 24,515 pts·m<sup>−3</sup> for B1 and B2, respectively. These volumetric point densities allowed the identification of micro-topographic features and very fine details (Figure 4a–d and Table 3). The point density was uniform in the area of interest as the result of a well-planned and executed convergent image network geometry (Figure 3). The error statistics estimated for B1 and B2 showed

an outstanding performance of the technique, with RMSEs always below 0.03 m (Table 3). On the other hand, the aerial SfM-MVS produced a lower density ( $39 \text{ pts}\cdot\text{m}^{-3}$ ) and a less-accurate ( $\text{RMSE}_{\text{CCP}} = 0.092 \text{ m}$ ) point cloud (Figure 4g,h).

**Table 3.** Characteristics of 3D point clouds produced by means of SfM-MVS photogrammetry (ponds B1, B2, and DBM) and the TLS instrument (pond P4). GSD: ground-sampling distance; GCP: ground control point; CCP: check control point; RMSE: root mean square error; ME: mean error; STD: standard deviation of error for CCP; UAV: unmanned aerial vehicle. \* Note that data for DBM refer to a larger study area and dataset used in Alfonso-Torreño et al. [66].

	B1	B2	DBM *	P4
Acquisition	Terrestrial	Terrestrial	Aerial (UAV)	Terrestrial
Images (n)	273	149	1257	-
GSD (cm)	0.93	1.52	4.00	-
Points (n)	59,884,444	95,499,578	171,757,830	158,918,500
Volumetric point density ( $\text{pts}\cdot\text{m}^{-3}$ )	19,143	24,515	39	58,366
GCP (n)	15	15	10	7
CCP (n)	5	5	5	1
$\text{RMSE}_{\text{GCP}}$ (m)	0.020	0.014	0.005	0.006
$\text{RMSE}_{\text{CCP}}$ (m)	0.016	0.016	0.092	0.009
$\text{RMSE}_{\text{CCP-x}}$ (m)	0.017	0.015	0.027	0.0138
$\text{RMSE}_{\text{CCP-y}}$ (m)	0.020	0.012	0.145	0.0164
$\text{RMSE}_{\text{CCP-z}}$ (m)	0.012	0.022	0.128	0.005
$\text{ME}_{\text{CCP}}$ (m)	0.008	0.007	-0.029	0.007
$\text{STD}_{\text{CCP}}$ (m)	0.004	0.015	0.094	0.007

The concurrent use of SfM-MVS and GNSS (for the submerged terrain) produced very accurate DEMs for the terrestrial datasets. The estimated  $\text{RMSE}_{\text{CCP-z}}$  for these DEMs resulted in an average error of 1.19% in the maximum volume estimation, varying from 0.72 to 1.65%. The  $\text{RMSE}_{\text{CCP-z}}$  for the DEM elaborated using the aerial SfM-MVS dataset and the GNSS was an order of magnitude larger ( $\text{RMSE}_{\text{CCP-z}} = 0.128 \text{ m}$ ) than the terrestrial approach, and resulted in an error of 12.15% in the estimation of the pond capacity. Note that the  $\text{RMSE}_{\text{CCP}}$  shown in Table 3 are a final independent validation of the resulting DEM surfaces. Therefore, this parameter included the interpolation error and the error associated to any technique used to produce the DEM (i.e., SfM-MVS photogrammetry and GNSS).

### 3.2. GNSS, TLS, and LIDAR

The RMSE of the locations surveyed by the GNSS at the submerged surface of the watering ponds varied from 0.007 m to 0.017 m (Table 4). These were expected figures for a widely used and tested surveying technique, and differences between ponds were not statistically significant. No spatial pattern was observed in the RMSE of the GNSS-surveyed locations, suggesting a uniform spatial distribution of errors. Note that the RMSE figures shown in Table 4 refer exclusively to the accuracy of the GNSS locations registered, while the interpolation errors of each DEM are shown as  $\text{RMSE}_z$  in Table 5. This parameter was calculated using independent CCPs (acquired also by means of the GNSS) and the DEMs that were used later to estimate  $V_{\text{max}}$  and  $A_{\text{max}}$  (Table 5).

The TLS produced by far the densest and most accurate data among the techniques and instruments used (Table 3). The average point density of the TLS-derived point cloud was  $58,366 \text{ pts}\cdot\text{m}^{-3}$ ; i.e., more than twice the estimated density of point clouds produced by the terrestrial SfM-MVS techniques. However, point densities were highly variable spatially, with larger values close to the TLS stations (Figure 4e,f). The average registration error of the different point clouds–stations of the TLS instrument was 0.002 m, varying from 0.0003 m to 0.008 m. However, the need to merge (and georeference) the TLS-acquired point cloud with the GNSS data recorded for the submerged terrain produced a degradation of

this accuracy to the GNSS range of errors (0.01–0.03 m). The DEM produced for pond P4 with the combination of TLS and GNSS showed a  $RMSE_z$  of 0.036 m that resulted in an error of 3.27% in the estimation of the maximum volume.

**Table 4.** Global navigation satellite system (GNSS) locations surveyed at each watering pond and the root mean square error (RMSE) estimated for the dataset.

Pond	Points (n)	RMSE (m)
B1	42	0.012
B2	28	0.015
B3	20	0.012
P1	55	0.017
P2	53	0.010
P3	33	0.007
P4	716	0.011
DBM	84	0.012

**Table 5.** Pond geometric characteristics estimated using the DEMs produced by the different geomatic approaches and propagated errors.  $A_{max}$ : maximum pond area;  $V_{max}$ : pond capacity;  $RMSE_z$ : vertical root mean square error;  $V_E$ : uncertainty of volume estimation. Note that the  $RMSE_z$  was calculated using check control points; i.e., points that were not used during the production of the DEM.

Pond	$V_{max}$ (m <sup>3</sup> )	$A_{max}$ (m <sup>2</sup> )	$RMSE_z$	$V_E$ (m <sup>3</sup> )	$V_E$ (%)
B1	2282	1711	0.022	37.65	1.65
B2	5151	2848	0.109	310.40	6.03
B3	3351	2006	0.012	24.07	0.72
P1	1680	1764	0.210	370.60	22.06
P2	4978	4916	0.110	540.80	10.86
P3	3635	3393	0.333	1129.80	31.08
P4	2158	1958	0.036	70.47	3.27
DBM	7575	6437	0.143	920.56	12.15

The watering ponds modelled using LIDAR and GNSS techniques showed a DEM with an  $RMSE_z$  that varied from 0.109 m to 0.333 m. These figures represented an average error of 17.51% in the estimation of the  $V_{max}$ , varying from 10.86% for pond P2 to 31.08% for pond P3.

### 3.3. Pond-Specific and Generalized V–A–h Models

Table 6 and Figure 6 show the pond-specific V–h, A–h, and V–A relationships that resulted for the study ponds when power and quadratic functions were fitted. In general, good fits could be obtained with both power and quadratic functions ( $R^2 > 0.9$ ), indicating that watering pond morphometry was adequately described by these types of functions. However, a significantly better performance of the quadratic functions was evidenced, especially for the V–h and A–h relationships. Thus, while a NRMSE greater than 10% was obtained in some ponds when the potential functions were used, this statistic rarely exceeded 2% with the quadratic functions (Table 6). These low errors were accompanied in all cases by excellent coefficients of determination ( $R^2 > 0.995$ ). Power functions gave rise to fits with such levels of goodness only in the case of V–A relationships, with  $R^2$  values higher than 0.99 and NRMSE around 5% (except for pond B3:  $R^2 = 0.985$ , NRMSE = 8.54%).

**Table 6.** Pond-specific V–h, A–h, and V–A relationships; coefficients of determination ( $R^2$ ); and normalized root mean square errors (NRMSE) that resulted from fitting power and quadratic functions to the V and A values derived from the DEM of each pond.

Pond	Power Functions			Quadratic Functions		
	Equation	$R^2$	NRMSE (%)	Equation	$R^2$	NRMSE (%)
V–h relationships						
B1	$V = 292.42 h^{2.035}$	0.998	2.14	$V = 274.18 h^2 + 51.05 h - 11.40$	1.000	0.20
B2	$V = 347.21 h^{2.239}$	0.995	6.23	$V = 327.07 h^2 + 118.45 h - 42.69$	1.000	0.54
B3	$V = 461.67 h^{2.256}$	0.990	7.82	$V = 432.72 h^2 + 282.88 h - 119.12$	0.999	0.80
P1	$V = 114.34 h^{3.363}$	0.956	15.98	$V = 386.61 h^2 - 339.83 h + 76.63$	0.998	1.26
P2	$V = 260.96 h^{2.491}$	0.998	3.55	$V = 742.72 h^2 - 841.35 h + 243.84$	0.997	1.56
P3	$V = 222.93 h^{2.611}$	0.992	4.18	$V = 672.19 h^2 - 651.76 h + 145.52$	0.999	0.78
P4	$V = 185.67 h^{3.081}$	0.983	14.37	$V = 415.24 h^2 - 172.99 h + 8.91$	0.997	1.59
DBM	$V = 1563.02 h^{2.036}$	0.979	4.97	$V = 1266.45 h^2 + 379.14 h - 26.50$	1.000	0.18
A–h relationships						
B1	$A = 594.03 h^{0.973}$	0.997	1.46	$A = 11.40 h^2 + 524.76 h + 50.89$	0.998	1.26
B2	$A = 719.37 h^{1.088}$	0.974	6.66	$A = -103.13 h^2 + 938.76 h - 44.85$	0.998	1.31
B3	$A = 974.90 h^{1.091}$	0.953	9.32	$A = -165.4 h^2 + 1427.5 h - 108.92$	0.997	1.65
P1	$A = 346.07 h^{2.037}$	0.943	9.27	$A = 203.09 h^2 + 231.00 h - 41.21$	0.999	1.02
P2	$A = 677.41 h^{1.554}$	0.990	5.42	$A = 470.60 h^2 + 18.28 h + 76.35$	0.996	1.70
P3	$A = 593.41 h^{1.687}$	0.980	2.94	$A = 235.14 h^2 + 620.48 h - 187.0$	0.995	2.24
P4	$A = 449.91 h^{1.906}$	0.976	11.75	$A = 89.97 h^2 + 613.87 h - 135.79$	0.998	1.51
DBM	$A = 2996.23 h^{0.870}$	0.972	2.12	$A = 88.29 h^2 + 2374.58 h + 418.02$	0.997	1.57
V–A relationships						
B1	$V = 0.00047 A^{2.090}$	0.999	3.33	$V = 0.00073 A^2 + 0.30 A - 94.02$	0.998	1.51
B2	$V = 0.00056 A^{2.027}$	0.992	5.72	$V = 0.00100 A^2 - 0.36 A + 42.32$	0.999	1.20
B3	$V = 0.00045 A^{2.015}$	0.985	8.54	$V = 0.00094 A^2 - 0.95 A + 264.34$	0.996	1.89
P1	$V = 0.00801 A^{1.636}$	0.996	0.78	$V = 0.00040 A^2 + 0.24 A - 7.45$	1.000	0.38
P2	$V = 0.00811 A^{1.593}$	0.996	5.67	$V = 0.00009 A^2 + 0.66 A - 145.41$	0.995	2.20
P3	$V = 0.01261 A^{1.532}$	0.992	4.60	$V = 0.00028 A^2 + 0.16 A - 11.42$	0.998	1.37
P4	$V = 0.01001 A^{1.609}$	0.998	4.15	$V = 0.00047 A^2 + 0.23 A - 20.49$	0.996	1.98
DBM	$V = 0.00001 A^{2.321}$	0.990	5.75	$V = 0.00016 A^2 + 0.19 A - 243.58$	0.999	0.94

Of the eight watering ponds analyzed, six (75%) had power V–h relationships in which the parameter  $\beta$  was less than 3 (Table 6), indicating that watering ponds tend to have concave bathymetries [67]. Also noteworthy, in the case of power functions, was the similarity of the adjustment parameters between ponds of the same farm (Table 6).

Regarding the generalized V–h, A–h, and V–A relationships (Table 7 and Figure 7), the resulting coefficients of determination and the NRMSE values were of similar magnitude for power and quadratic functions. In general, the fits were quite poor in the case of the generalized V–h and A–h relationships. However, relatively good fits could be obtained for the generalized V–A relationships, especially when the quadratic function was used ( $R^2 = 0.863$  and NRMSE values ranging between 5% and 18%; Table 7).

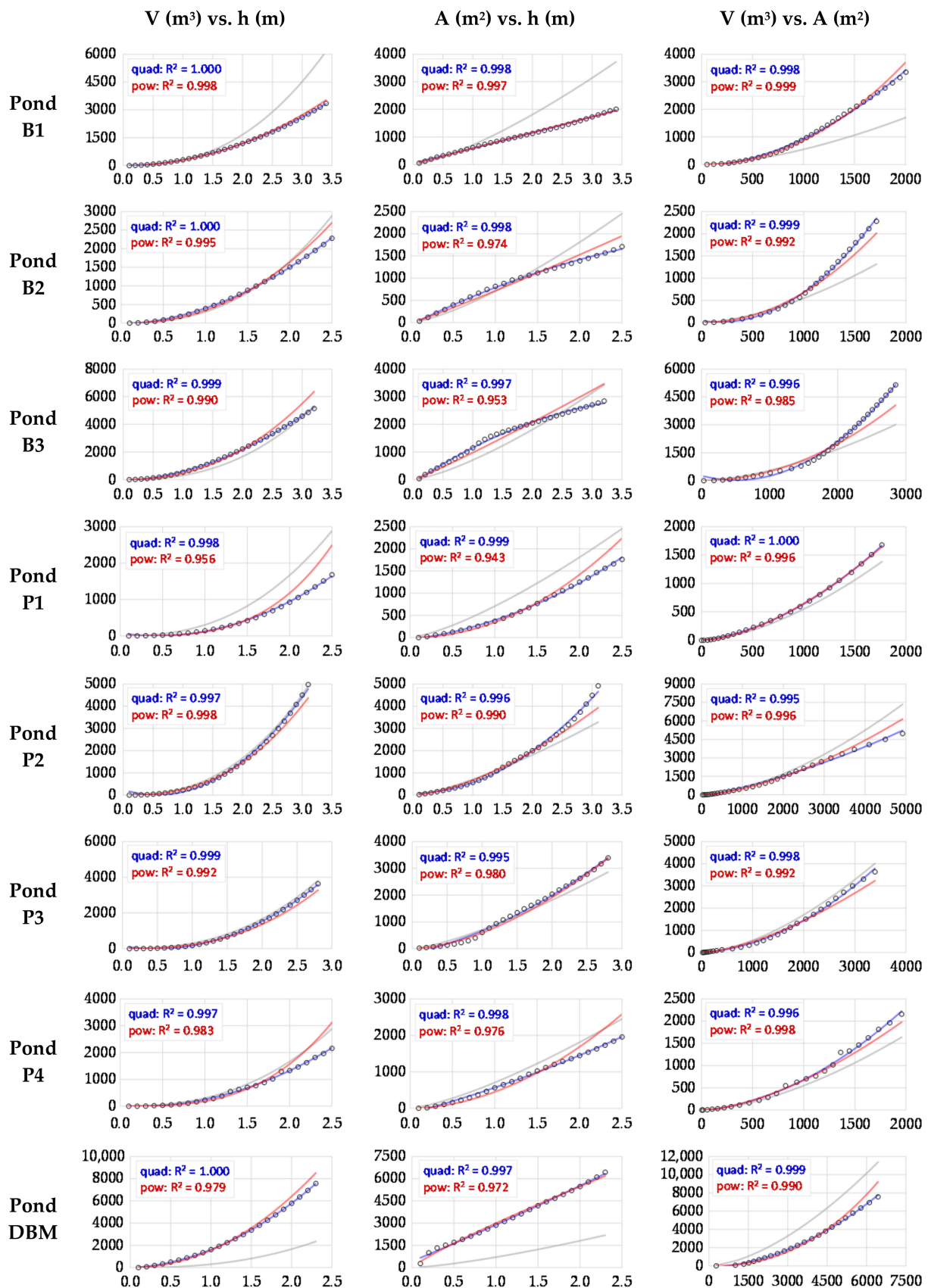
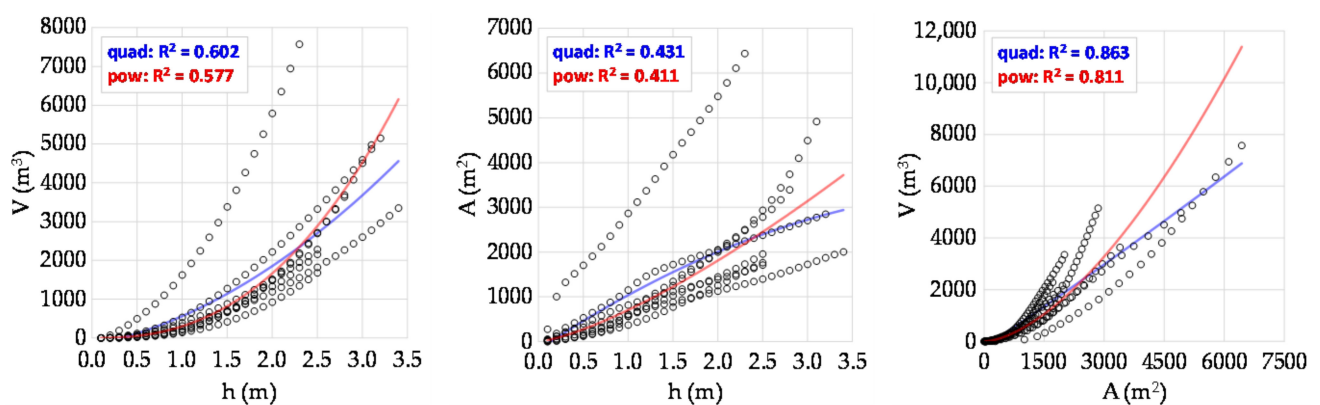


Figure 6. Pond-specific V-h, A-h, and V-A relationships that resulted from fitting power functions (red lines) and quadratic functions (blue lines) to the V and A values (black dots) derived from the DEM of each pond. The corresponding generalized V-h, A-h, and V-A relationships are also shown (gray lines).

**Table 7.** Generalized V–h, A–h, and V–A relationships and coefficients of determination ( $R^2$ ) that resulted from fitting power and quadratic functions to the DEM-derived V and A values of all ponds. The normalized root mean square errors (NRMSE) when the generalized relationships were used to estimate the V and A values of each pond are also indicated.

Pond	Power Functions			Quadratic Functions		
	Equation	$R^2$	NRMSE (%)	Equation	$R^2$	NRMSE (%)
Generalized V–h	$V = 302.16 h^{2.463}$	0.577		$V = 267.64 h^2 + 488.40 h - 192.85$	0.602	
B1			32.72			20.60
B2			8.83			11.16
B3			6.77			9.13
P1			32.67			39.47
P2			2.60			8.02
P3			3.66			8.57
P4			13.12			18.21
DBM			34.67			32.66
Generalized A–h	$A = 707.32 h^{1.357}$	0.411		$A = -124.95 h^2 + 1342.53 h - 178.97$	0.431	
B1			42.18			37.04
B2			18.66			24.83
B3			12.40			3.42
P1			24.30			35.72
P2			10.42			14.05
P3			6.74			10.27
P4			13.57			23.41
DBM			41.56			38.27
Generalized V–A	$V = 0.0071 A^{1.629}$	0.811		$V = 10^{-5} A^2 + 1.04 A - 234.20$	0.863	
B1			22.21			17.18
B2			18.36			12.45
B3			16.93			17.92
P1			6.72			7.92
P2			13.29			5.28
P3			5.04			8.62
P4			11.02			7.14
DBM			27.52			11.74



**Figure 7.** Generalized V–h, A–h, and V–A relationships that resulted from fitting power functions (red lines) and quadratic functions (blue lines) to the DEM-derived V and A values (black dots) of all ponds.

### 3.4. Generalized V–A Relationships for Estimating Water-Storage Capacity

Figure 8a presents the generalized  $V_{max}$ – $A_{max}$  relationship derived from the  $V_{max}$  and  $A_{max}$  values of the study ponds, expressed by the following equation:

$$V_{max} = 2.453 \times A_{max}^{0.913}, \quad (6)$$

where  $V_{max}$  and  $A_{max}$  are expressed in  $m^3$  and  $m^2$ , respectively. This function fitted the data reasonably well ( $R^2 = 0.83$ ), although the volumetric errors, when used to estimate the maximum capacity of the ponds, were highly variable (Table 8), ranging from  $-2.4\%$  (pond DBM) to  $34.9\%$  (pond P1), and being the average of the absolute values of  $17.7\%$ . In any case, these estimates were more accurate than those obtained using the generalized V–A relationships derived from the complete geometry of the ponds, whose equations are shown in Table 7. With the latter, whether adjusted by using power functions or quadratic functions, the errors associated with estimating the maximum capacity of the ponds reached values above  $40\%$  in many cases (Table 8).

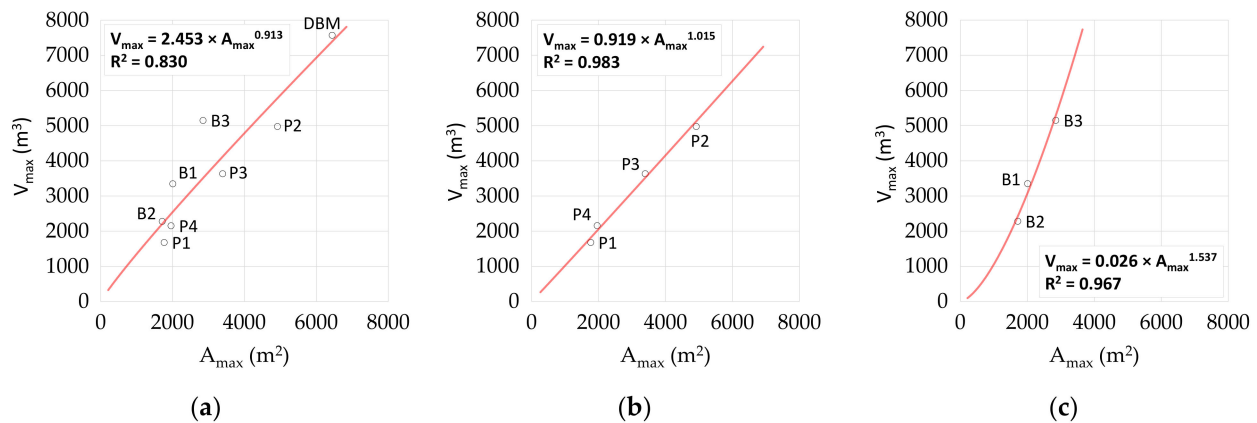


**Figure 8.** (a) Generalized  $V_{max}$ – $A_{max}$  relationship derived from the  $V_{max}$  and  $A_{max}$  values of the study ponds; and resulting farm-specific  $V_{max}$ – $A_{max}$  relationships for (b) Parapuños and (c) La Brava. Note that we only had data from a single pond in Dehesa Boyal Monroy, so it was not possible to obtain a specific  $V_{max}$ – $A_{max}$  relationship for this farm.

**Table 8.** Maximum pond capacities ( $V_{max}$ ) estimated using the generalized V–A (power and quadratic) relationships, the generalized  $V_{max}$ – $A_{max}$  relationship, and the farm-specific  $V_{max}$ – $A_{max}$  relationships; and associated volumetric errors ( $V_E$ ) in relation to the  $V_{max}$  values obtained from the DEMs.

Pond	DEM	Generalized V–A (Power)		Generalized V–A (Quadratic)		Generalized $V_{max}$ – $A_{max}$		Farm-Specific $V_{max}$ – $A_{max}$	
	$V_{max}$ ( $m^3$ )	$V_{max}$ ( $m^3$ )	$V_E$ (%)	$V_{max}$ ( $m^3$ )	$V_E$ (%)	$V_{max}$ ( $m^3$ )	$V_E$ (%)	$V_{max}$ ( $m^3$ )	$V_E$ (%)
B1	3351	1704	−49.15	1896	−43.43	2547	−23.97	3084	−7.97
B2	2282	1316	−42.34	1578	−30.84	2204	−3.43	2416	5.88
B3	5151	3016	−41.45	2814	−45.37	3509	−31.88	5286	2.62
P1	1680	1383	−17.66	1636	−2.64	2267	34.91	1811	7.79
P2	4978	7342	47.48	5130	3.05	5779	16.08	5122	2.89
P3	3635	4012	10.37	3416	−6.03	4118	13.28	3515	−3.30
P4	2158	1638	−24.08	1844	−14.54	2492	15.49	2012	−6.75
DBM	7574	11387	50.35	6887	−9.07	7391	−2.41	-	-

Interestingly, very good fits were found at the farm level ( $R^2 > 0.96$  and  $|V_E| < 8\%$ ; Figure 8b,c and Table 8), which suggested that some factors acting at that scale were relevant in determining the morphometry of the ponds.

#### 4. Discussion

The combination of terrestrial SfM–MVS photogrammetry (for the emerged terrain) and GNSS (for the submerged terrain) proved to produce accurate topographic models of small watering ponds, with errors in the range of 1–3 cm. These findings were in agreement with other specific previous applications of the SfM–MVS technique to reconstruct similar features (topographic depressions), such as channels or gully headcuts, also using convergent image network geometries [68,69].

The use of the GNSS to support and to complement the SfM-MVS technique was necessary in our study areas due to several reasons. The first was that, even at the end of the summer, watering ponds usually show a thick layer of water at the bottom, which is usually turbid [70] and makes unsuitable underwater photo-reconstructions such as those carried out successfully in other environments [71]. The second reason was that the photogrammetric model needed to be (at least) scaled using GCPs (or GNSS RTK systems connected to the camera instead of GCPs; e.g., [72]), while the GNSS allowed the survey of additional CCPs to independently quantify the accuracy of the model. In recent years, affordable (or low-cost) GNSS survey-grade devices have been available in the market [73] to carry out this task. For example, the two antennas (rover and base station) used here (Emlid Reach RS, Figure 3a) have a price of  $\approx$  EUR 800 (each), and they may be controlled with any smartphone or tablet device. The last reason was that, even without water, the incidence angle that resulted from the hand-held-camera acquisition approach and the almost flat topography of the bottom of watering ponds (Figure 2a) may have been glancing, reducing the number and density of tie points [74] and influencing the accuracy of marking GCPs and CCPs [75]. The use of the GNSS to cover the submerged terrain is well known in the literature and produces accurate bathymetric models [76]. However, GNSS surveys are time-consuming, and point densities are usually lower than those of laser-based or photogrammetric technologies, as evidenced in our study.

The development of SfM-MVS photogrammetry in the last decade has democratized the use and production of high-resolution DEMs [77]. The present application shows that models produced by this technique may provide accurate estimations of pond topography and storage capacity. Once the DEM is produced and the V–A–h relationships are determined for a specific pond, a permanent surveying rod would be sufficient to know the volume of water stored in almost real time. The availability of this data may lead to a better farm management, particularly in water-limited environments such as dehesas [3]. The use of terrestrial SfM-MVS and GNSS, instead of LIDAR and GNSS, represents an important improvement, as it reduces errors in an order of magnitude, allowing the accurate estimation of water stored in the ponds even in periods with low levels.

Our results indicated that the use of existing LIDAR datasets in combination with GNSS only provided rough estimations of water-storage capacity and were particularly unsuitable in periods of water scarcity, when errors were larger than the amount of water stored.

In the complete absence of water in the pond, the use of UAV platforms in combination with SfM-MVS photogrammetry may become an effective alternative that overcomes the glancing perspective of the hand-held camera in the terrestrial approach [74]. In this sense, UAVs that integrate RTK or post-processing kinematic (PPK) systems on board are a promising technology that may reduce the time-consuming and labor-intensive task of GCP–CCP acquisition [78]. Any approach supported on GNSS data acquisition should balance number, spatial extent, and point density. For instance, GNSS devices are suitable to model the flat and horizontal bottom of the ponds, but unsuitable to survey steep and rough banks.

The TLS is the instrument that produces the most accurate and densest point clouds; however, the need to register the submerged terrain or to georeference the resulting models will degrade the accuracy to that of the georeferencing technique or instruments [79]; for example, GNSS systems. Experiences of shallow-water bathymetry in conjunction with emerged ground surveying by means of TLS instruments are scarce and limited to specific hydraulic and water-quality conditions [49], which is not the case for watering ponds in the SW Iberian Peninsula.

On the other hand, the resulting TLS point clouds commonly show heterogeneous point densities (larger close to stations) and occlusions due to the line-of-sight effect [69]. The TLS coverage may be improved by increasing the number of TLS locations [69], which is not always efficient, as the setup of the equipment and data acquisition may take approximately 30 min for each station, and the resulting cloud may show unnecessarily

high point densities in other regions. Additionally, the cost of the equipment is still an important limitation for most users [79]. The camera-based SfM-MVS method provides better coverage in very complex topography or rough surfaces [69,80]. On the other hand, there are some experiences that open the door to the use of a single TLS to survey submerged and emerged terrain, but only under specific hydraulic and physical water-quality conditions [49], and this is not the case for watering ponds in the study area.

#### 4.1. Suitability of V–A–h Models to Describe Watering Pond Morphometry

This study demonstrated that simple analytical models based on quadratic or power functions can suitably describe watering-pond morphometry. The low associated errors allow these models to be used in hydrological simulation studies. Nonetheless, for simulation models using V–h and A–h relationships, we recommend the fits to be carried out preferably with quadratic functions, for which the NRMSE was less than 2% in almost all watering ponds in our study (Table 6). If V–A relationships are used, both power and quadratic functions would be appropriate (NRMSE rarely exceeded 6% in either case). The high coefficients of determination ( $R^2$ ) obtained for the pond-specific V–A–h models were in line with those reported for small reservoirs in other regions [81,82].

In an attempt to develop a V–A–h model that could be applied to non-surveyed watering ponds in the region, generalized V–h, A–h, and V–A relationships were derived from the bathymetries of the studied ponds. In general, the high NRMSE values obtained for these relationships (up to 42%; Table 7) evidenced the inconvenience of using regional V–A–h relationships as geometric models in hydrological simulation studies of individual watering ponds. However, relatively high  $R^2$  values were obtained for the generalized V–A relationships ( $R^2 > 0.8$ ; Table 7), which offers the possibility of using such relationships as geometric models of non-surveyed ponds in basin-wide studies, where the individual errors in the regionalization tend to cancel out at the basin scale [83].

In a previous study carried out in the SW Iberian Peninsula, Marín-Comitre et al. [3] obtained a generalized V–A relationship for livestock watering ponds in the region, expressed by the following power function:

$$V = 0.0031 \times A^{1.793}, \quad (7)$$

where V and A are expressed in  $m^3$  and  $m^2$ , respectively. The coefficients of this equation are similar to those obtained in this study for the generalized (power) V–A relationship (Table 7). However, it should be noted that Equation (7) was derived using only three watering ponds from two different farms. Therefore, the new V–A relationships obtained here, based on eight watering ponds from three different farms, represent a significant improvement compared to that expressed by Equation (7).

#### 4.2. Performance of V–A Relationships for Estimating Water Storage Capacity in Watering Ponds

It is known that the V–A relationships of small reservoirs are region-specific and that they vary with the geomorphology and geology of the area [13,50,51]. The local nature of these relationships was confirmed by our results, since similar pond-specific V–A relationships were found between ponds of the same farm (Table 6), while significant differences were found between the equations obtained for each of the farm-specific  $V_{max}$ – $A_{max}$  relationships (Figure 8b,c). However, these last differences were greater than expected considering the similarity of the geomorphological and geological conditions between the different study areas, which suggested that other factors acting at the farm level were relevant in determining the morphometry of the ponds. For example, the pond construction methodology could play a decisive role.

Nonetheless, we investigated whether a generalized V–A relationship obtained using several reference watering ponds from various locations could be reliably used to estimate the storage capacity of non-surveyed ponds at the regional scale. For this purpose, V–A relationships can be constructed either using only the values of maximum volume ( $V_{max}$ ) and maximum flooded area ( $A_{max}$ ) from the reference water bodies [10,50,56,67,84,85] or using

the volume and area values over the entire depth range of the water bodies [3,12,13,81]. After testing both methods, it was found that the relationship derived from the  $V_{max}$  and  $A_{max}$  data (Equation (6)) led to lower errors in the estimation of the pond capacities (Table 8) than the generalized V–A relationships (shown in Table 7), even though similar coefficients of determination were obtained in all cases (around 0.8).

Therefore, we propose the  $V_{max}$ – $A_{max}$  relationship expressed by Equation (6) to be used to estimate the storage capacity of watering ponds at the regional level. The  $R^2$  value of 0.83 was comparable to those reported by previous studies for generalized V–A relationships in other regions [11,50,56] and gave, to some extent, confidence in its use, especially for watering ponds lacking other available information. The average volumetric error associated with these estimates amounted to 17.7%, with maximum values above 30% for some ponds (Table 8). This means that the pond capacities estimated from the flooded areas might be inaccurate when those are considered individually. However, it is expected that the individual errors tend to cancel out when the relationships are used for broad-based applications carried out at the basin or regional scale [83], in which a large number of ponds are involved. Ultimately, the proposed relationship can be a useful tool for decision-making procedures when managing water resources in rangeland farms of the SW Iberian Peninsula.

## 5. Conclusions

The combination of terrestrial SfM–MVS photogrammetry and GNSS produced accurate topographic models of small watering ponds that were useful to improve existing V–A relationships. These models were suitable to accurately estimate  $V_{max}$ , comparable to those produced using TLS+GNSS. The errors of the DEMs and  $V_{max}$  estimations produced by the rest of the techniques were, at least, an order of magnitude larger.

Pond-specific V–A–h relationships based on quadratic or power functions can adequately describe watering pond morphometry and may be used reliably as geometric models of ponds in hydrological simulation studies.

A generalized V–A relationship was obtained from the surveys carried out at eight small watering ponds from three representative rangeland farms in the SW Iberian Peninsula that may be used to estimate the storage capacity of other watering ponds in this region.

**Author Contributions:** Conceptualization, Ubaldo Marín-Comitre and Álvaro Gómez-Gutiérrez; data curation, Ubaldo Marín-Comitre, Álvaro Gómez-Gutiérrez, Manuel Sánchez-Fernández, and Alberto Alfonso-Torreño; formal analysis, Ubaldo Marín-Comitre, Álvaro Gómez-Gutiérrez, and Francisco Lavado-Contador; funding acquisition, Álvaro Gómez-Gutiérrez and Francisco Lavado-Contador; investigation, Ubaldo Marín-Comitre, Álvaro Gómez-Gutiérrez, and Alberto Alfonso-Torreño; methodology, Ubaldo Marín-Comitre, Álvaro Gómez-Gutiérrez, and Manuel Sánchez-Fernández; project administration, Álvaro Gómez-Gutiérrez and Francisco Lavado-Contador; software, Ubaldo Marín-Comitre, Álvaro Gómez-Gutiérrez, Manuel Sánchez-Fernández, and Alberto Alfonso-Torreño; supervision, Álvaro Gómez-Gutiérrez and Francisco Lavado-Contador; Validation, Ubaldo Marín-Comitre and Álvaro Gómez-Gutiérrez; visualization, Ubaldo Marín-Comitre, Álvaro Gómez-Gutiérrez, and Alberto Alfonso-Torreño; writing—original draft, Ubaldo Marín-Comitre and Álvaro Gómez-Gutiérrez; writing—review and editing, Ubaldo Marín-Comitre, Álvaro Gómez-Gutiérrez, and Francisco Lavado-Contador. All authors have read and agreed to the published version of the manuscript.

**Funding:** This publication has been made possible thanks to funding granted by the Consejería de Economía, Ciencia y Agenda Digital from Junta de Extremadura, and the European Regional Development Fund of the European Union through the reference grants IB20036, GR18037, and GR18053.

**Institutional Review Board Statement:** Not applicable.

**Informed Consent Statement:** Not applicable.

**Data Availability Statement:** Publicly available LIDAR datasets were analyzed in this study. This data can be found here: <https://centrodedescargas.cnig.es/CentroDescargas/index.jsp> (accessed on 24 July 2021).

**Conflicts of Interest:** The authors declare no conflict of interest. The funders had no role in the design of the study; in the collection, analyses, or interpretation of data; in the writing of the manuscript; or in the decision to publish the results.

## References

- Pulido-Fernández, M.; Schnabel, S. La disponibilidad de agua en explotaciones de ganadería extensiva. In *Aportaciones a la Geografía Física de Extremadura con Especial Referencia a las Dehesas*; Schnabel, S., Lavado-Contador, F., Gómez-Gutiérrez, A., García-Marín, R., Eds.; Fundicotex: Cáceres, Spain, 2010; pp. 221–235. (In Spanish)
- Camacho, J.; Sánchez, E.; Aguilar, F.; Gómez, A.; Lozano, A. *Manual Práctico de Balsas Agrícolas. Diseño y Gestión Para su Mejora Ambiental*; Consejería de Medio Ambiente (Junta de Andalucía): Sevilla, Spain, 2011. (In Spanish)
- Marín-Comitre, U.; Schnabel, S.; Pulido-Fernández, M. Hydrological Characterization of Watering Ponds in Rangeland Farms in the Southwest Iberian Peninsula. *Water* **2020**, *12*, 1038. [CrossRef]
- Rosenberry, D.O.; Hayashi, M. Assessing and Measuring Wetland Hydrology. In *Wetland Techniques*; Anderson, J.T., Davis, C.A., Eds.; Springer: Dordrecht, The Netherlands, 2013; Volume 1, pp. 87–225.
- Hayashi, M.; van der Kamp, G. Water level changes in ponds and lakes: The hydrological processes. In *Plant Disturbance Ecology. The Process and the Response*; Johnson, E.A., Miyaniishi, K., Eds.; Academic Press: San Diego, CA, USA, 2007; pp. 311–339.
- O'Connor, D.J. Seasonal and long-term variations of dissolved solids in lakes and reservoirs. *J. Environ. Eng.* **1989**, *115*, 1213–1234. [CrossRef]
- Wise, W.R.; Annable, M.D.; Walser, J.A.E.; Switt, R.S.; Shaw, D.T. A wetland–aquifer interaction test. *J. Hydrol.* **2000**, *227*, 257–272. [CrossRef]
- Trigg, M.A.; Cook, P.G.; Brunner, P. Groundwater fluxes in a shallow seasonal wetland pond: The effect of bathymetric uncertainty on predicted water and solute balances. *J. Hydrol.* **2014**, *517*, 901–912. [CrossRef]
- Mishra, V.; Cherkauer, K.A.; Bowling, L.C. Parameterization of Lakes and Wetlands for Energy and Water Balance Studies in the Great Lakes Region. *J. Hydrometeorol.* **2010**, *11*, 1057–1082. [CrossRef]
- Liebe, J.R.; Van De Giesen, N.; Andreini, M.; Walter, M.T.; Steenhuis, T.S. Determining watershed response in data poor environments with remotely sensed small reservoirs as runoff gauges. *Water Resour. Res.* **2009**, *45*. [CrossRef]
- Hughes, D.A.; Mantel, S.K. Estimating the uncertainty in simulating the impacts of small farm dams on streamflow regimes in South Africa. *Hydrol. Sci. J.* **2010**, *55*, 578–592. [CrossRef]
- Gal, L.; Grippa, M.; Hiernaux, P.; Peugeot, C.; Mougin, E.; Kergoat, L. Changes in lakes water volume and runoff over ungauged Sahelian watersheds. *J. Hydrol.* **2016**, *540*, 1176–1188. [CrossRef]
- Ogilvie, A.; Belaud, G.; Massuel, S.; Mulligan, M.; Le Goulven, P.; Calvez, R. Assessing floods and droughts in ungauged small reservoirs with long-term landsat imagery. *Geosciences* **2016**, *6*, 42. [CrossRef]
- Neitsch, S.L.; Arnold, J.G.; Kiniry, J.R.; Williams, J.R. *Soil and Water Assessment Tool: Theoretical documentation (Version 2009)*; Texas Water Resources Institute: College Station, TX, USA, 2011.
- Los Huertos, M.; Smith, D. Wetland bathymetry and mapping. In *Wetland Techniques*; Anderson, J.T., Davis, C.A., Eds.; Springer: Dordrecht, The Netherlands, 2013; Volume 1, pp. 49–86.
- Hohenthal, J.; Alho, P.; Hyypä, J.; Hyypä, H. Laser scanning applications in fluvial studies. *Prog. Phys. Geogr. Earth Environ.* **2011**, *35*, 782–809. [CrossRef]
- CNIG. Centro de descargas del Centro Nacional de Información Geográfica (CNIG). Ministerio de Transportes, Movilidad y Agenda Urbana, Government of Spain. (In Spanish). Available online: <https://centrodedescargas.cnig.es/CentroDescargas/index.jsp> (accessed on 4 June 2021).
- Langhammer, J.; Janský, B.; Kocum, J.; Minařík, R. 3-D reconstruction of an abandoned montane reservoir using UAV photogrammetry, aerial LiDAR and field survey. *Appl. Geogr.* **2018**, *98*, 9–21. [CrossRef]
- Rhee, D.S.; Kim, Y.D.; Kang, B.; Kim, D. Applications of unmanned aerial vehicles in fluvial remote sensing: An overview of recent achievements. *KSCE J. Civ. Eng.* **2018**, *22*, 588–602. [CrossRef]
- Rusnák, M.; Sládek, J.; Kidová, A.; Lehotský, M. Template for high-resolution river landscape mapping using UAV technology. *Measurement* **2018**, *115*, 139–151. [CrossRef]
- Bailly, J.-S.; Le Coarer, Y.; Languille, P.; Stigermark, C.-J.; Allouis, T. Geostatistical estimations of bathymetric LiDAR errors on rivers. *Earth Surf. Process. Landf.* **2010**, *35*, 1199–1210. [CrossRef]
- Raineault, N.A.; Trembanis, A.C.; Miller, D.C. Mapping Benthic Habitats in Delaware Bay and the Coastal Atlantic: Acoustic Techniques Provide Greater Coverage and High Resolution in Complex, Shallow-Water Environments. *Estuaries Coasts* **2012**, *35*, 682–699. [CrossRef]
- Smith, M.; Vericat, D.; Gibbins, C. Through-water terrestrial laser scanning of gravel beds at the patch scale. *Earth Surf. Process. Landf.* **2012**, *37*, 411–421. [CrossRef]
- Kurowski, M.; Thal, J.; Damerius, R.; Korte, H.; Jeinsch, T. Automated Survey in Very Shallow Water using an Unmanned Surface Vehicle. *IFAC PapersOnLine* **2019**, *52*, 146–151. [CrossRef]
- Burdziakowski, P.; Specht, C.; Dabrowski, P.S.; Specht, M.; Lewicka, O.; Makar, A. Using UAV Photogrammetry to Analyse Changes in the Coastal Zone Based on the Sopot Tombolo (Salient) Measurement Project. *Sensors* **2020**, *20*, 4000. [CrossRef] [PubMed]

26. Genchi, S.A.; Vitale, A.J.; Perillo, G.M.E.; Seitz, C.; Delrieux, C.A. Mapping Topobathymetry in a Shallow Tidal Environment Using Low-Cost Technology. *Remote Sens.* **2020**, *12*, 1394. [[CrossRef](#)]
27. Specht, M.; Specht, C.; Mindykowski, J.; Dąbrowski, P.; Mańnicki, R.; Makar, A. Geospatial Modeling of the Tombolo Phenomenon in Sopot using Integrated Geodetic and Hydrographic Measurement Methods. *Remote Sens.* **2020**, *12*, 737. [[CrossRef](#)]
28. Stateczny, A.; Kazimierski, W.; Burdziakowski, P.; Motyl, W.; Wisniewska, M. Shore Construction Detection by Automotive Radar for the Needs of Autonomous Surface Vehicle Navigation. *ISPRS Int. J. Geo Inf.* **2019**, *8*, 80. [[CrossRef](#)]
29. Kedzierski, M.; Wilińska, M.; Wierzbicki, D.; Fryskowska, A.; Deliś, P. Image data fusion for flood plain mapping. In Proceedings of the 9th International Conference Environmental Engineering (9th Icee)—Selected Papers, Vilnius, Lithuania, 22–23 May 2014. [[CrossRef](#)]
30. Gao, H.; Birkett, C.; Lettenmaier, D.P. Global monitoring of large reservoir storage from satellite remote sensing. *Water Resour. Res.* **2012**, *48*. [[CrossRef](#)]
31. Sima, S.; Tajrishy, M. Using satellite data to extract volume–area–elevation relationships for Urmia Lake, Iran. *J. Great Lakes Res.* **2013**, *39*, 90–99. [[CrossRef](#)]
32. Song, C.; Huang, B.; Ke, L. Modeling and analysis of lake water storage changes on the Tibetan Plateau using multi-mission satellite data. *Remote Sens. Environ.* **2013**, *135*, 25–35. [[CrossRef](#)]
33. Smith, L.C.; Pavelsky, T.M. Remote sensing of volumetric storage changes in lakes. *Earth Surf. Process. Landf.* **2009**, *34*, 1353–1358. [[CrossRef](#)]
34. Lu, S.; Ouyang, N.; Wu, B.; Wei, Y.; Tesemma, Z. Lake water volume calculation with time series remote-sensing images. *Int. J. Remote Sens.* **2013**, *34*, 7962–7973. [[CrossRef](#)]
35. Birkett, C.M. Synergistic remote sensing of Lake Chad Variability of basin inundation. *Remote Sens. Environ.* **2000**, *72*, 218–236. [[CrossRef](#)]
36. Duan, Z.; Bastiaanssen, W.G.M. Estimating water volume variations in lakes and reservoirs from four operational satellite altimetry databases and satellite imagery data. *Remote Sens. Environ.* **2013**, *134*, 403–416. [[CrossRef](#)]
37. Baup, F.; Frappart, F.; Maubant, J. Combining high-resolution satellite images and altimetry to estimate the volume of small lakes. *Hydrol. Earth Syst. Sci.* **2014**, *18*, 2007–2020. [[CrossRef](#)]
38. De Graaf, G.; Kamal, M.; Martin, T.; Schepel, M. Remote sensing techniques for detecting and mapping aquaculture ponds in Bangladesh. In Proceedings of the Second International Symposium on GIS-Spatial Analyses in Fishery and Aquatic Sciences, Brighton, UK, 3–6 September 2002; pp. 3–6.
39. Jones, K.; Lanthier, Y.; van der Voet, P.; van Valkengoed, E.; Taylor, D.; Fernández-Prieto, D. Monitoring and assessment of wetlands using Earth Observation: The GlobWetland project. *J. Environ. Manag.* **2009**, *90*, 2154–2169. [[CrossRef](#)]
40. Gallant, A.L. The Challenges of Remote Monitoring of Wetlands. *Remote Sens.* **2015**, *7*, 10938–10950. [[CrossRef](#)]
41. Ogilvie, A.; Belaud, G.; Massuel, S.; Mulligan, M.; Le Goulven, P.; Calvez, R. Surface water monitoring in small water bodies: Potential and limits of multi-sensor Landsat time series. *Hydrol. Earth Syst. Sci.* **2018**, *22*, 4349–4380. [[CrossRef](#)]
42. Ullman, S. Interpretation of structure from motion. *Proc. R. Soc. London Ser. B Biol. Sci.* **1979**, *203*, 405–426. [[CrossRef](#)]
43. Seitz, S.M.; Curless, B.; Diebel, J.; Scharstein, D.; Szeliski, R. A comparison and evaluation of multi-view stereo reconstruction algorithms. In Proceedings of the 2006 IEEE Computer Society Conference on Computer Vision and Pattern Recognition (CVPR'06), New York, NY, USA, 17–22 June 2006; pp. 519–528.
44. Castillo, C.; Pérez, R.; James, M.R.; Quinton, J.N.; Taguas, E.V.; Gomez, J.A. Comparing the Accuracy of Several Field Methods for Measuring Gully Erosion. *Soil Sci. Soc. Am. J.* **2012**, *76*, 1319–1332. [[CrossRef](#)]
45. Chandler, J.; Fryer, J. Autodesk 123D catch: How accurate is it. *Geomat. World* **2013**, *2*, 28–30.
46. Fonstad, M.A.; Dietrich, J.T.; Courville, B.C.; Jensen, J.L.; Carbonneau, P.E. Topographic structure from motion: A new development in photogrammetric measurement. *Earth Surf. Process. Landf.* **2013**, *38*, 421–430. [[CrossRef](#)]
47. James, M.R.; Robson, S. Straightforward reconstruction of 3D surfaces and topography with a camera: Accuracy and geoscience application. *J. Geophys. Res. Earth Surf.* **2012**, *117*. [[CrossRef](#)]
48. Woodget, A.S.; Carbonneau, P.E.; Visser, F.; Maddock, I.P. Quantifying submerged fluvial topography using hyperspatial resolution UAS imagery and structure from motion photogrammetry. *Earth Surf. Process. Landf.* **2015**, *40*, 47–64. [[CrossRef](#)]
49. Smith, M.W.; Vericat, D. Evaluating shallow-water bathymetry from through-water terrestrial laser scanning under a range of hydraulic and physical water quality conditions. *River Res. Appl.* **2014**, *30*, 905–924. [[CrossRef](#)]
50. Rodrigues, L.N.; Sano, E.E.; Steenhuis, T.S.; Passo, D.P. Estimation of Small Reservoir Storage Capacities with Remote Sensing in the Brazilian Savannah Region. *Water Resour. Manag.* **2012**, *26*, 873–882. [[CrossRef](#)]
51. Habets, F.; Molénat, J.; Carluet, N.; Douez, O.; Leenhardt, D. The cumulative impacts of small reservoirs on hydrology: A review. *Sci. Total Environ.* **2018**, *643*, 850–867. [[CrossRef](#)] [[PubMed](#)]
52. Gleason, R.A.; Tangen, B.A.; Laubhan, M.K.; Kermes, K.E.; Euliss, N.H., Jr. *Estimating Water Storage Capacity of Existing and Potentially Restorable Wetland Depressions in a Subbasin of the Red River of the North: U.S. Geological Survey Open-File Report 2007–1159*; U.S. Geological Survey: Reston, VA, USA, 2007.
53. Lowe, L.; Nathan, R.; Morden, R. Assessing the impact of farm dams on streamflows, Part II: Regional characterisation. *Australas. J. Water Resour.* **2005**, *9*, 13–26. [[CrossRef](#)]
54. Fowler, K.; Morden, R.; Lowe, L.; Nathan, R. Advances in assessing the impact of hillside farm dams on streamflow. *Australas. J. Water Resour.* **2015**, *19*, 96–108. [[CrossRef](#)]

55. Huang, S.L.; Young, C.; Feng, M.; Heidemann, K.; Cushing, M.; Mushet, D.M.; Liu, S.G. Demonstration of a conceptual model for using LiDAR to improve the estimation of floodwater mitigation potential of Prairie Pothole Region wetlands. *J. Hydrol.* **2011**, *405*, 417–426. [[CrossRef](#)]
56. Wiens, L.H. A Surface Area-Volume Relationship for Prairie Wetlands in the Upper Assiniboine River Basin, Saskatchewan. *Can. Water Resour. J. Rev. Can. Ressour. Hydr.* **2001**, *26*, 503–513. [[CrossRef](#)]
57. Annor, F.O.; van de Giesen, N.; Liebe, J.; van de Zaag, P.; Tilmant, A.; Odai, S.N. Delineation of small reservoirs using radar imagery in a semi-arid environment: A case study in the upper east region of Ghana. *Phys. Chem. Earth Parts A/B/C* **2009**, *34*, 309–315. [[CrossRef](#)]
58. Soti, V.; Puech, C.; Seen, D.L.; Bertran, A.; Vignolles, C.; Mondet, B.; Dessay, N.; Tran, A. The potential for remote sensing and hydrologic modelling to assess the spatio-temporal dynamics of ponds in the Ferlo Region (Senegal). *Hydrol. Earth Syst. Sci.* **2010**, *14*, 1449–1464. [[CrossRef](#)]
59. Huang, S.; Young, C.; Abdul-Aziz, O.I.; Dahal, D.; Feng, M.; Liu, S. Simulating the water budget of a Prairie Potholes complex from LiDAR and hydrological models in North Dakota, USA. *Hydrol. Sci. J.* **2013**, *58*, 1434–1444. [[CrossRef](#)]
60. Jones, S.K.; Fremier, A.K.; DeClerck, F.A.; Smedley, D.; Pieck, A.O.; Mulligan, M. Big Data and Multiple Methods for Mapping Small Reservoirs: Comparing Accuracies for Applications in Agricultural Landscapes. *Remote Sens.* **2017**, *9*, 1307. [[CrossRef](#)]
61. Garrido, P.; Elbakidze, M.; Angelstam, P.; Plieninger, T.; Pulido, F.; Moreno, G. Stakeholder perspectives of wood-pasture ecosystem services: A case study from Iberian dehesas. *Land Use Policy* **2017**, *60*, 324–333. [[CrossRef](#)]
62. Schnabel, S.; Dahlgren, R.A.; Moreno-Marcos, G. Soil and Water Dynamics. In *Mediterranean Oak Woodland Working Landscapes: Dehesas of Spain and Ranchlands of California*; Campos, P., Huntsinger, L., Oviedo, J.L., Starrs, P.F., Diaz, M., Standiford, R.B., Montero, G., Eds.; Springer: Dordrecht, The Netherlands, 2013; pp. 91–121.
63. Schnabel, S.; Gómez-Gutiérrez, Á. The role of interannual rainfall variability on runoff generation in a small dry sub-humid watershed with disperse tree cover. *Cuad. Investig. Geogr.* **2013**, *39*. [[CrossRef](#)]
64. Plieninger, T.; Hartel, T.; Martin-Lopez, B.; Beaufoy, G.; Bergmeier, E.; Kirby, K.; Montero-Parejo, M.J.; Moreno, G.; Oteros-Rozas, E.; Van Uytvanck, J. Wood-pastures of Europe: Geographic coverage, social–ecological values, conservation management, and policy implications. *Biol. Conserv.* **2015**, *190*, 70–79. [[CrossRef](#)]
65. Hutchinson, M.F. Calculation of hydrologically sound digital elevation models. In Proceedings of the Third International Symposium on Spatial Data Handling, Sidney, Australia, 17–19 August 1988; pp. 117–133.
66. Alfonso-Torreño, A.; Gómez-Gutiérrez, Á.; Schnabel, S.; Contador, J.F.L.; Blasco, J.J.D.S.; Sánchez-Fernández, M. sUAS, SfM-MVS photogrammetry and a topographic algorithm method to quantify the volume of sediments retained in check-dams. *Sci. Total Environ.* **2019**, *678*, 369–382. [[CrossRef](#)]
67. Molle, F. Caractéristiques et Potentialités des açudes du Nordeste Brésilien. Ph.D. Thesis, Université de Montpellier, Montpellier, France, 1991. (In French)
68. Gómez-Gutiérrez, A.; Schnabel, S.; Berenguer-Sempere, F.; Contador, J.F.L.; Delgado, J.R. Using 3D photo-reconstruction methods to estimate gully headcut erosion. *Catena* **2014**, *120*, 91–101. [[CrossRef](#)]
69. Gómez-Gutiérrez, A.; Biggs, T.; Elizondoa, N.G.; Errea, P.; Alonso-González, E.; Romero, E.N.; Blasco, J.J.D.S. Using visibility analysis to improve point density and processing time of SfM-MVS techniques for 3D reconstruction of landforms. *Earth Surf. Process. Landf.* **2020**, *45*, 2524–2539. [[CrossRef](#)]
70. Marín-Comitre, U.; Schnabel, S.; Barrera-González, J.; Pulido-Fernández, M. Pond water quality for livestock in southwestern Iberian rangelands. *Rangel. Ecol. Manag.* (under review).
71. Visser, F.; Woodget, A.; Skellern, A.; Forsey, J.; Warburton, J.; Johnson, R. An evaluation of a low-cost pole aerial photography (PAP) and structure from motion (SfM) approach for topographic surveying of small rivers. *Int. J. Remote Sens.* **2019**, *40*, 9321–9351. [[CrossRef](#)]
72. Jaud, M.; Bertin, S.; Beauverger, M.; Augereau, E.; Delacourt, C. RTK GNSS-Assisted Terrestrial SfM Photogrammetry without GCP: Application to Coastal Morphodynamics Monitoring. *Remote Sens.* **2020**, *12*, 1889. [[CrossRef](#)]
73. Odolinski, R.; Teunissen, P.J.G. Single-frequency, dual-GNSS versus dual-frequency, single-GNSS: A low-cost and high-grade receivers GPS-BDS RTK analysis. *J. Geod.* **2016**, *90*, 1255–1278. [[CrossRef](#)]
74. Jaud, M.; Letortu, P.; Théry, C.; Grandjean, P.; Costa, S.; Maquaire, O.; Davidson, R.; Le Dantec, N. UAV survey of a coastal cliff face—Selection of the best imaging angle. *Measurement* **2019**, *139*, 10–20. [[CrossRef](#)]
75. Gómez-Gutiérrez, Á.; Gonçalves, G.R. Surveying coastal cliffs using two UAV platforms (multirotor and fixed-wing) and three different approaches for the estimation of volumetric changes. *Int. J. Remote Sens.* **2020**, *41*, 8143–8175. [[CrossRef](#)]
76. Wheaton, J.M.; Brasington, J.; Darby, S.E.; Sear, D.A. Accounting for uncertainty in DEMs from repeat topographic surveys: Improved sediment budgets. *Earth Surf. Process. Landf.* **2010**, *35*, 136–156. [[CrossRef](#)]
77. Smith, M.W.; Carrivick, J.L.; Quincey, D.J. Structure from motion photogrammetry in physical geography. *Prog. Phys. Geogr. Earth Environ.* **2016**, *40*, 247–275. [[CrossRef](#)]
78. Turner, I.L.; Harley, M.D.; Drummond, C.D. UAVs for coastal surveying. *Coast. Eng.* **2016**, *114*, 19–24. [[CrossRef](#)]
79. Telling, J.; Lyda, A.; Hartzell, P.; Glennie, C. Review of Earth science research using terrestrial laser scanning. *Earth Sci. Rev.* **2017**, *169*, 35–68. [[CrossRef](#)]

80. Nouwakpo, S.K.; Weltz, M.A.; McGwire, K.C. Assessing the performance of structure-from-motion photogrammetry and terrestrial LiDAR for reconstructing soil surface microtopography of naturally vegetated plots. *Earth Surf. Process. Landf.* **2016**, *41*, 308–322. [[CrossRef](#)]
81. Sawunyama, T.; Senzanje, A.; Mhizha, A. Estimation of small reservoir storage capacities in Limpopo River Basin using geographical information systems (GIS) and remotely sensed surface areas: Case of Mzingwane catchment. *Phys. Chem. Earth Parts A/B/C* **2006**, *31*, 935–943. [[CrossRef](#)]
82. Ogilvie, A. Upscaling Water Availability and Water Use Assessments in Hydro-Social Systems: The Small Reservoirs of The Merguellil Catchment (Central Tunisia). Ph.D. Thesis, Université de Montpellier, Montpellier, France, 2015.
83. Fowler, K.; Donohue, R.; Morden, R.; Durrant, J.; Hall, J. Decision support and uncertainty in self-supply irrigation areas. In *Proceedings of the 34th Hydrology and Water Resources Symposium 2012, Sydney, Australia, 19–22 December 2012*; Engineers Australia: Barton, ACT, Australia, 2012; pp. 93–101.
84. Liebe, J.; van de Giesen, N.; Andreini, M. Estimation of small reservoir storage capacities in a semi-arid environment—A case study in the Upper East Region of Ghana. *Phys. Chem. Earth Parts A/B/C* **2005**, *30*, 448–454. [[CrossRef](#)]
85. Karran, D.J.; Westbrook, C.J.; Wheaton, J.M.; Johnston, C.A.; Bedard-Haughn, A. Rapid surface-water volume estimations in beaver ponds. *Hydrol. Earth Syst. Sci.* **2017**, *21*, 1039–1050. [[CrossRef](#)]